

# Behaviour of the Serre Equations in the Presence of Steep Gradients Revisited

J.P.A. Pitt<sup>a,\*</sup>, C. Zoppou<sup>a</sup>, S.G. Roberts<sup>a</sup>

<sup>a</sup>*Mathematical Sciences Institute, Australian National University, Canberra, ACT 0200, Australia*

---

## Abstract

*Keywords:* Serre equations, steep gradients, dam break

---

### 1. Introduction

2      The behaviour of steep gradients in a flow is important to shallow water modelling  
3 both because there are problems in which steep gradients are present in the initial con-  
4 ditions such as the propagation of a bore or the classical dam-break problem and also  
5 because some problems develop steep gradients as they evolve such as shoaling waves  
6 on a beach.

7      For the Serre equations there are no analytic solutions to problems containing steep  
8 gradients. Expressions for the leading wave height and speed of an undular bore were  
9 derived and verified for a range of different undular bores [1]. However, to infer the  
10 structure of solutions to problems containing steep gradients we resort to numerical  
11 methods.

12     Unfortunately there are few examples in the literature which depict the behaviour  
13 of numerical solutions to the Serre equations in the presence of steep gradients [1, 2,  
14 3, 4]. These papers all present problems with discontinuous initial conditions [2] or a  
15 smooth approximation to them [1, 3, 4]. Among these papers there are differences in  
16 the structures of the numerical solutions implying different natures of the true solutions  
17 of the Serre equations. Although, for the dam-break problem the analytic solution of  
18 the shallow water wave equations has been demonstrated to capture the mean behaviour  
19 of numerical solutions of the Serre equations despite smoothing of the initial conditions  
20 [2, 3].

21     The aim of this paper is to investigate the effect of smoothing the initial condi-  
22 tions on the structure of the numerical solutions of the Serre equations and assess the  
23 usefulness of the analytic solution of the shallow water wave equations as well as the  
24 Whitham modulation results of El et al. [1]. This is achieved by comparing the results

---

\*Corresponding author

Email addresses: jordan.pitt@anu.edu.au (J.P.A. Pitt),  
christopher.zoppou@anu.edu.au (C. Zoppou), stephen.roberts@anu.edu.au  
(S.G. Roberts)

of five different numerical schemes. Three of which are the first, second and third-order methods presented by Zoppou et al. [5] where this first-order method is equivalent to the method of Le Métayer et al. [2]. The fourth method is a recreation of the second-order method used by El et al. [1]. Lastly the fifth method is a complete second-order finite difference approximation to the Serre equations.

These five methods were all used to solve a smooth approximation to the dam-break problem with the same heights as El et al. [1] and Le Métayer et al. [2] to investigate the differences among the structures of the published numerical solutions. It was found that the results of [2] were dominated by the diffusion of their first-order numerical method. While the results for the other papers were impacted by the smoothing of the initial conditions [1, 3, 4]. Through this process a new structure of the numerical solutions was found which has hitherto not been published. It was confirmed that the analytic solutions for the shallow water wave equations are a good guide for the mean behaviour of the numerical solutions. While the Whitham modulation results of El et al. [1] agree with our numerical solutions, and offer a better prediction of the speed of the bore than the shallow water wave equations.

The paper is organised as follows: The Serre equations are given, the numerical methods are described briefly with details left to the Appendix, then a smoothed approximation to the dam-break problem is presented and lastly the results of our numerical investigation into the behaviour of the Serre equations applied to the dam-break problem are presented.

## 2. Serre Equations

The Serre equations can be derived by integrating the full incompressible Euler equations over the water depth, see for example [6]. They can also be derived as an asymptotic expansion of the Euler equations, see for example [7]. Assuming a constant horizontal bed the one-dimensional Serre equations are [8]

$$\frac{\partial h}{\partial t} + \frac{\partial(uh)}{\partial x} = 0 \quad (1a)$$

and

$$\underbrace{\frac{\partial(uh)}{\partial t} + \frac{\partial}{\partial x} \left( u^2 h + \frac{gh^2}{2} \right)}_{\text{Shallow Water Wave Equations}} + \underbrace{\frac{\partial}{\partial x} \left( \frac{h^3}{3} \left[ \frac{\partial u}{\partial x} \frac{\partial u}{\partial x} - u \frac{\partial^2 u}{\partial x^2} - \frac{\partial^2 u}{\partial x \partial t} \right] \right)}_{\text{Dispersion Terms}} = 0. \quad (1b)$$

Serre Equations

Where  $u$  is the horizontal velocity over the depth of water  $h$ ,  $g$  is the acceleration due to gravity,  $x$  is the horizontal spatial variable and  $t$  is time.

### 2.1. Conservation

The Serre equations are conservation laws for mass ( $h$ ) and momentum ( $uh$ ) [6]. The Serre equations admit a Hamiltonian [9, 10]

$$\mathcal{H}(x, t) = \frac{1}{2} \left( hu^2 + \frac{h^3}{3} \left( \frac{\partial u}{\partial x} \right)^2 + gh^2 \right) \quad (2)$$

63 which represents the energy for the Serre equations and is conserved. The total amount  
 64 of a quantity  $q$  in a system occurring on the interval  $[a, b]$  is measured by

$$65 \quad C_q(t) = \int_a^b q(x, t) dx.$$

66 Conservation of a quantity  $q$  implies that  $C_q(0) = C_q(t) \forall t$  provided the interval is  
 67 fixed and the system is closed. Our numerical methods should have this conservation  
 68 property for  $h$ ,  $uh$  and  $\mathcal{H}$ .

### 70 3. Numerical Methods

71 Five numerical schemes are used to solve the Serre equations. The first ( $\mathcal{V}_1$ ), sec-  
 72 ond ( $\mathcal{V}_2$ ) and third-order ( $\mathcal{V}_3$ ) methods of [5], the method of El et al. [1] ( $\mathcal{E}$ ) and a  
 73 second-order finite difference method ( $\mathcal{G}$ ). These methods all use a fixed grid in time  
 74 and space, with subscripts denoting spatial indices and superscripts denoting time in-  
 75 dices. Thus for a quantity  $q$  on our grid  $q_i^n = q(x_i, t^n)$  with the grids uniform such that  
 76  $\Delta x = x_i - x_{i-1} \forall i$  and  $\Delta t = t^n - t^{n-1} \forall n$ . A cell is a particularly useful unit of the finite  
 77 volume method, the  $i$ th cell is the interval  $[x_i - \Delta x/2, x_i + \Delta x/2]$  centered around  $x_i$ .

78 All methods are stable under the CFL condition [11] and have demonstrated the  
 79 appropriate order of convergence for smooth problems [5]. Furthermore,  $\mathcal{V}_2$  and  $\mathcal{V}_3$   
 80 have been validated against experimental data containing steep gradients [5]. For com-  
 81 pleteness the two methods  $\mathcal{G}$  and  $\mathcal{E}$  which are not explicitly published are presented in  
 82 the Appendix to allow for replication.

### 83 4. Smoothed Dam Break Problem

84 In the literature the dam-break problem is usually approximated by a smooth hy-  
 85 perbolic tangent function [3, 4]. Such an approximation will be called a smoothed  
 86 dam-break problem and will be defined by

$$87 \quad h(x, 0) = h_0 + \frac{h_1 - h_0}{2} \left( 1 + \tanh\left(\frac{x_0 - x}{\alpha}\right) \right), \quad (3a)$$

$$88 \quad u(x, 0) = 0.0m/s. \quad (3b)$$

90 Where  $\alpha$  measures the distance over which 46.117% of the smooth transition between  
 91 the two heights of  $h_0$  and  $h_1$  centred around  $x_0$  occurs. Figure 1 demonstrates the  
 92 effect of varying  $\alpha$  for the smoothed dam-break problem with  $h_1 = 1.8m$ ,  $h_0 = 1m$  and  
 93  $x_0 = 500m$ . These are the same  $h_0$  and  $h_1$  values as those of the dam-breaks presented  
 94 by [1] and [2] and will be the values used in Sections 4 and 5.

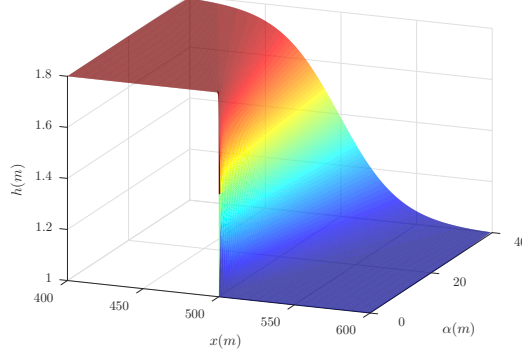


Figure 1: Initial conditions for the smooth dam-break problem with  $h_0 = 1m$ ,  $h_1 = 1.8m$  and  $x_0 = 500m$  as  $\alpha$  varies.

#### 97    4.1. Measures and Comparisons

98    There are no analytic results for the Serre equations for either the discontinuous  
 99    dam-break problem or its smoothed approximation. To assess the validity of our results  
 100   we must resort to other comparisons such as measuring the error in the conservation  
 101   of the conserved quantities and measuring the distance between numerical solutions as  
 102    $\Delta x \rightarrow 0$ . Le Métayer et al. [2] and Mitsotakis et al. [3] demonstrated that the analytic  
 103   solution of the shallow water wave equations for the dam-break problem captures the  
 104   mean behaviour of their numerical results. El et al. [1] noted the presence of an impor-  
 105   tant location termed a ‘degenerate contact discontinuity’ in their numerical solutions  
 106   and derived expressions for the leading wave height and speed of an undular bore in  
 107   the Serre equations. We make use of all of these measures, comparisons and important  
 108   locations in Section 5 and so we present some relevant background for each here.

##### 109    4.1.1. Conserved Quantities

110   The initial conditions of the smoothed dam-break (3) were integrated to get the  
 111   following expressions for  $C_h(0)$ ,  $C_{uh}(0)$  and  $C_H(0)$  provided  $x_0$  is the midpoint of the  
 112   spatial domain  $[a, b]$  in which the smoothed dam-break occurs

113                 
$$C_h(0) = \frac{h_1 + h_0}{2} (b - a),$$
  
 114  
 115

116                 
$$C_{uh}(0) = 0$$

118   and

119                 
$$C_H(0) = \frac{g}{4} \left( h_0^2 - h_1^2 + \alpha (h_1 - h_0)^2 \tanh \left( \frac{a - b}{2\alpha} \right) \right).$$
  
 120  
 121

122   To calculate the total amount of a quantity  $q$  in our numerical solution we fit a  
 123   quartic interpolant of the primitive variables  $h$  and  $u$  over a cell utilising neighbouring

124 cells and then apply Gaussian quadrature with 3 points to get the total amount of  $q$  in a  
 125 cell and then sum this for all cells to get the total amount of  $q$  in our numerical solution  
 126 at time  $t$  which we call  $C_q^*(t)$ . We then measure the error in conservation of a quantity  
 127  $q$  for a numerical method by

$$128 \quad C_1^q = \frac{|C_q(0) - C_q^*(t)|}{|C_q(0)|}. \quad (5)$$

129

130 Note that for  $uh$  the denominator is 0 and that there is a flux of momentum due to the  
 131 unequal heights at both ends of the domain. To resolve these issues for  $uh$  we measure  
 132 the error in the conservation of  $uh$  by

$$133 \quad C_1^{uh} = \left| C_{uh}(0) - C_{uh}^*(t) - \frac{gt}{2} (h(b)^2 - h(a)^2) \right|. \quad (6)$$

134

#### 135 4.1.2. Distance between Numerical Results

136 By measuring the relative distance between numerical solutions we can assess  
 137 whether our numerical solutions are converging as  $\Delta x \rightarrow 0$ . Rather than comparing  
 138 all numerical results to one another we simplify by comparing all our numerical sol-  
 139 lutions to the one with the smallest  $\Delta x$ . For some quantity  $q$  we have a numerical  
 140 approximation to it  $q'$  at the locations  $x_i$  and our numerical approximation to it with  
 141 smallest  $\Delta x$   $q^*$  at the locations  $x_j$ . By using grids such that for each  $i$  there is a  $j^*(i)$   
 142 such that  $x_i = x_{j^*(i)}$  and summing the difference for each  $i$

$$143 \quad L_1^q = \frac{\sum_i |q'_i - q_{j^*(i)}^*|}{\sum_i |q_{j^*(i)}^*|} \quad (7)$$

144

145 we can measure the relative distance between these numerical solutions on the grid  $x_i$ .

#### 146 4.1.3. Shallow Water Wave Equation Analytic Solution for the Dam Break

147 For the discontinuous dam break problem the shallow water wave equations which  
 148 are the Serre equations with dispersive terms neglected can be solved analytically. The  
 149 analytic solution of the shallow water wave equations has been used as a comparative  
 150 tool against numerical results in the literature [2, 3] as they appear to capture the mean  
 151 behaviour of the numerical solutions.

152 An example of the analytic solution of the shallow water wave equations for the  
 153 dam-break problem is presented in Figure 3 at  $t = 30s$ . Region I is the undisturbed  
 154 water upstream of the dam-break at constant height ( $h_1$ ) and velocity (0m/s) and region  
 155 II is the rarefaction fan connecting regions I and III. Regions III and IV are the constant  
 156 height ( $h_2$ ) and constant velocity ( $u_2$ ) state which are separated by  $x_{u_2} = x_0 + u_2 t$  and  
 157 region V is the undisturbed water downstream at constant height ( $h_0$ ) and velocity  
 158 (0m/s) separated from region IV by a shock which travels at velocity  $S_2$ . Expressions  
 159 for the unknown quantities  $h_2$ ,  $u_2$  and  $S_2$  in terms of  $h_0$  and  $h_1$  were given by Wu et al.  
 160 [12]

$$161 \quad h_2 = \frac{h_0}{2} \left( \sqrt{1 + 8 \left( \frac{2h_2}{h_2 - h_0} \frac{\sqrt{gh_1} - \sqrt{gh_2}}{\sqrt{gh_0}} \right)^2} - 1 \right), \quad (8a)$$

162

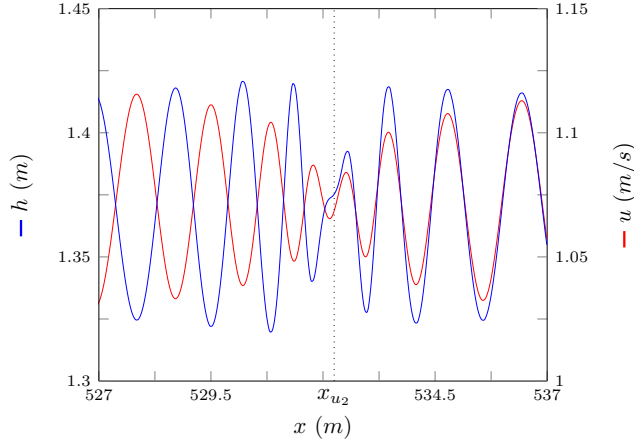


Figure 2:  $h$  (—) and  $u$  (—) for numerical solution of the smooth dam-break by  $\mathcal{V}_3$  with  $\alpha = 0.1m$  and  $\Delta x = 10/2^9 m$  at  $t = 30s$  around contact discontinuity.

$$163 \quad 164 \quad u_2 = 2\left(\sqrt{gh_1} - \sqrt{gh_2}\right) \quad (8b)$$

165 and

$$166 \quad 167 \quad S_2 = \frac{h_2 u_2}{h_2 - h_0}. \quad (8c)$$

168 From these values the location of the shock separating regions IV and V at time  $t$  is  
169  $x_{S_2}(t) = x_0 + S_2 t$ . Applying (8) to our dam-break problem heights results in  $h_2 =$   
170  $1.36898m$ ,  $u_2 = 1.074975 m/s$  and  $S_2 = 3.98835 m/s$  which are demonstrated in  
171 Figure 3.

#### 172 4.1.4. Contact Discontinuity

173 El et al. [1] noted the presence of a ‘degenerate contact discontinuity’ in their nu-  
174 matical solutions which travels at the mean velocity in the bore and has zero amplitude.  
175 The structure around this point is the central difference between the numerical results in  
176 the literature with most demonstrating a constant height state around this point [2, 3, 4]  
177 and El et al. [1] reporting oscillations around it.

178  $h$  and  $u$  reveal another property of the contact discontinuity, that it is the transition  
179 between when  $h$  and  $u$  are anti-phase to the left and when  $h$  and  $u$  are in-phase to the  
180 right. A plot of  $h$  and  $u$  around the contact discontinuity at  $x_{u_2}$  is presented in Figure 2  
181 for  $\mathcal{V}_3$ ’s numerical solution of a smoothed dam-break problem with  $\alpha = 0.1m$ .

182 Inspecting the phase velocity for the linearised Serre equations

$$183 \quad 184 \quad v_p = u \pm \sqrt{gh} \sqrt{\frac{3}{h^2 k^2 + 3}} \quad (9)$$

185 with wave number  $k$ , it can be seen that as  $k \rightarrow \infty$  then  $v_p \rightarrow u$  and as  $k \rightarrow 0$  then  
186  $v_p \rightarrow u \pm \sqrt{gh}$ . Therefore since the contact discontinuity travels at the means bore speed

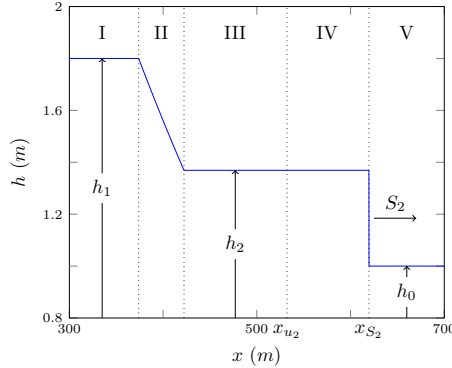


Figure 3: Analytic solution at  $t = 30$ s of the shallow water wave equations for the dam-break problem with  $h_0 = 1m$ ,  $h_1 = 1.8m$  and  $x_0 = 100m$ .

187  $u$  it corresponds to large wave numbers. Therefore when  $u$  and  $h$  are anti-phase this cor-  
 188 responds to the negative branch of the phase velocity  $u - \sqrt{gh} \sqrt{3/(h^2k^2 + 3)}$  and when  
 189  $u$  and  $h$  are in-phase this corresponds to the positive branch  $u + \sqrt{gh} \sqrt{3/(h^2k^2 + 3)}$ .  
 190 This behaviour of  $h$  and  $u$  means that waves appear to be generated at the contact dis-  
 191 continuity and travel away from it. The contact discontinuity is at  $x_{u_2}$  because initially  
 192 it is located at  $x_0$  and  $u_2$  is a good approximation of the mean velocity inside a bore  
 193 [2, 3] and thus the speed of the contact discontinuity.

194 **4.1.5. Whitham Modulation for Undular Bores of the Serre Equations**

195 Undular bores for the one dimensional Serre equations were analysed by [1] and an  
 196 expression for the amplitude ( $A^+$ ) and speed ( $S^+$ ) of the leading wave of a bore shown  
 197 in Figure 4 were given

$$198 \quad \frac{\Delta}{(A^+ + 1)^{1/4}} - \left( \frac{3}{4 - \sqrt{A^+ + 1}} \right)^{21/10} \left( \frac{2}{1 + \sqrt{A^+ + 1}} \right)^{2/5} = 0 \quad (10a)$$

200 and

$$201 \quad S^+ = \sqrt{g(A^+ + 1)} \quad (10b)$$

where  $\Delta = h_b/h_0$ , and  $h_b$  is the amplitude of the bore. From this we define  $x_{S^+}(t) = x_0 + S^+t$  which is the location of the leading wave at time  $t$ . The height of the bore created by the dam-break in (10) used by El et al. [1] was

$$h_b = \frac{1}{4} \left( \sqrt{\frac{h_1}{h_0}} + 1 \right)^2.$$

203 Thus for our dam-break problem  $h_b = 1.37082\text{ m}$ ,  $\Delta = 1.37082$ ,  $A^+ = 1.73998\text{ m}$  and  
 204  $S^+ = 4.13148\text{ m/s}$ .

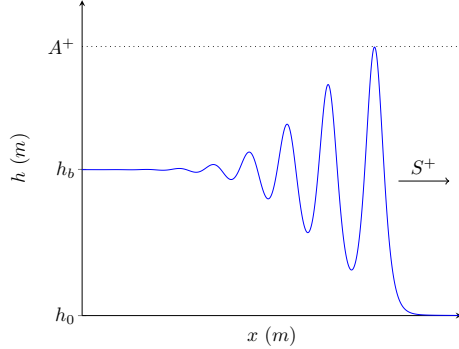


Figure 4: Demonstration of quantities obtained by Whitham modulation for undular bores of the Serre equations.

205 **5. Numerical Results**

206 We begin by looking into the effect of the initial steepness of the smoothed dam-  
 207 break problem for different  $\alpha$  values by observing what happens as  $\Delta x \rightarrow 0$  and our  
 208 numerical solutions better approximate the true solution of the Serre equations. To  
 209 have the smallest error we use the highest order well validated model  $\mathcal{V}_3$  in the fol-  
 210 lowing investigation. From these results we then investigate numerical results for long  
 211 time scales, how the shallow water wave equations analytic solution and El's Whitham  
 212 modulation values compare to our results and then finally present some other findings  
 213 about the behaviour of our numerical solutions.

214 All numerical methods used  $\Delta t = 0.01\Delta x$  which is smaller than required by the  
 215 CFL condition [11] which ensures stability of our schemes or the relation used by El  
 216 et al. [1].  $\Delta t$  was chosen to be smaller than necessary because for a final time of  $t = 30s$   
 217 making  $\Delta t$  small suppresses errors without excessively increasing the run-time of the  
 218 experiments.  $\mathcal{V}_2$  requires an input parameter to its slope limiter and this was chosen to  
 219 be  $\theta = 1.2$  [5].

220 *5.1. Observed Structures of the Numerical Solutions*

221 We observe that there are four different structures as  $\Delta x \rightarrow 0$  depending on the  
 222  $\alpha$  and the numerical method. The four structures are identified by the nature of the  
 223 solutions around  $x_{u_2}$  when  $\Delta x$  is small and they correspond to different structures in the  
 224 numerical solutions presented in the literature. For brevity the only given examples of  
 225 these structures will be the solutions of  $\mathcal{V}_3$  at  $t = 30s$  on the interval  $x \in [0m, 1000m]$   
 226 although they all also occurred for the numerical results of  $\mathcal{E}$ ,  $\mathcal{G}$  and  $\mathcal{V}_2$  using the same  
 227  $\alpha$  and  $\Delta x = 10/2^{10}m$ . All of the numerical methods presented use Dirichlet boundary  
 228 conditions with  $u = 0m/s$  at both boundaries and  $h = 1.8m$  on the left and  $h = 1m$  on  
 229 the right.

230 *5.1.1. Non-oscillatory Structure*

231 The first structure which will be referred to as the non-oscillatory structure is the  
 232 result of a large  $\alpha$ . When  $\alpha$  is large enough for the smoothed dam-break problem the

$\alpha (m)$	$\Delta x (m)$	$C_1^h$	$C_1^{uh}$	$C_1^H$	$L_1^h$	$L_1^u$
40	$10/2^4$	$2.0 \times 10^{-11}$	$1.8 \times 10^{-6}$	$1.2 \times 10^{-8}$	$1.7 \times 10^{-7}$	$2.9 \times 10^{-6}$
40	$10/2^{10}$	$1.8 \times 10^{-11}$	$2.2 \times 10^{-8}$	$3.6 \times 10^{-11}$	$2.5 \times 10^{-11}$	$6.5 \times 10^{-11}$
2	$10/2^4$	$4.9 \times 10^{-14}$	$5.1 \times 10^{-3}$	$8.7 \times 10^{-4}$	$5.0 \times 10^{-3}$	$6.8 \times 10^{-2}$
2	$10/2^{10}$	$4.0 \times 10^{-12}$	$5.0 \times 10^{-9}$	$2.0 \times 10^{-8}$	$1.8 \times 10^{-7}$	$2.3 \times 10^{-6}$
0.4	$10/2^4$	$9 \times 10^{-14}$	$4.8 \times 10^{-3}$	$1.0 \times 10^{-3}$	$6.8 \times 10^{-3} \dagger$	$9.9 \times 10^{-2} \dagger$
0.4	$10/2^{10}$	$3.9 \times 10^{-12}$	$5.0 \times 10^{-9}$	$2.0 \times 10^{-8}$	$3.6 \times 10^{-7} \dagger$	$5.0 \times 10^{-6} \dagger$
0.1	$10/2^4$	$7.6 \times 10^{-14}$	$4.8 \times 10^{-3}$	$1.0 \times 10^{-3}$	$7.0 \times 10^{-3} \dagger$	$1.0 \times 10^{-1} \dagger$
0.1	$10/2^{10}$	$3.9 \times 10^{-12}$	$4.6 \times 10^{-8}$	$7.6 \times 10^{-7}$	$5.0 \times 10^{-7} \dagger$	$6.4 \times 10^{-6} \dagger$

Table 1: All errors in conservation  $C_1^q$  (6) for the conserved quantities and relative distances  $L_1^q$  (7) of the primitive variables for numerical solutions of  $\mathcal{V}_3$ .  $L_1^q$  uses the numerical solution with  $\Delta x = 10/2^{11}m$  as the high resolution basis of comparison and  $\dagger$  indicates where the interval  $[520m, 540m]$  has been omitted from the comparison.

fluid to the left of  $x_0$  flows to fill the right side, but since  $\alpha$  is large the front of this flow is not steep enough to generate undulations over short time spans. Eventually the front of this flow steepens due to non-linearity and undulations develop there.

This structure is not present in the literature as no authors chose large enough  $\alpha$ . An example of this structure can be seen in Figure 5 for  $\alpha = 40m$  using  $\mathcal{V}_3$ , this structure was also observed for  $\mathcal{V}_1$ 's numerical solutions. Because this is a very smooth problem we observe that all numerical results are visually identical for all  $\Delta x < 10/2^4m$ . We note that  $\mathcal{V}_3$ 's numerical solution has  $h(x_{u_2}) > h_2$  and because no undulations are present the results of El et al. [1] are not applicable to these solutions.

From Table 1 it can be seen that the numerical solutions of  $\mathcal{V}_3$  conserve the conserved quantities very well for this particular  $\alpha$  for both  $\Delta x$ 's, although the smaller  $\Delta x$ 's numerical results are superior.  $C_1^{uh}$  is the worst performing of the measures because the smoothed dam-break has such a large transition width that  $h(0m) \neq 1.8m$  and  $h(1000m) \neq 1m$  causing small flows at the boundaries meaning the system is not closed.

These measures verify that we are converging as  $\Delta x \rightarrow 0$  and our solutions are relatively conservative as the errors for the highest resolution results except for  $C_1^{uh}$  are all at round-off error for each cells value as there are 100,000 cells. Therefore the numerical result in Figure 5 is an accurate representation of the behaviour of the Serre equations when  $\alpha$  is sufficiently large and in particular  $\alpha = 40m$ .

### 5.1.2. Flat Structure

The second structure will be referred to as the flat structure due to the presence of a constant height around  $x_{u_2}$ , this is the most common structure observed in the literature [2, 3, 4]. This structure consists of oscillations in regions III and IV which are separated by a constant height state around  $x_{u_2}$ . An example of the structure can be seen in the numerical solutions presented in Figure 6 when  $\alpha = 2m$ , this structure was also observed for  $\mathcal{V}_1$ 's solutions.

As  $\Delta x$  decreases the numerical solutions converge so that by  $\Delta x = 10/2^8m$  the

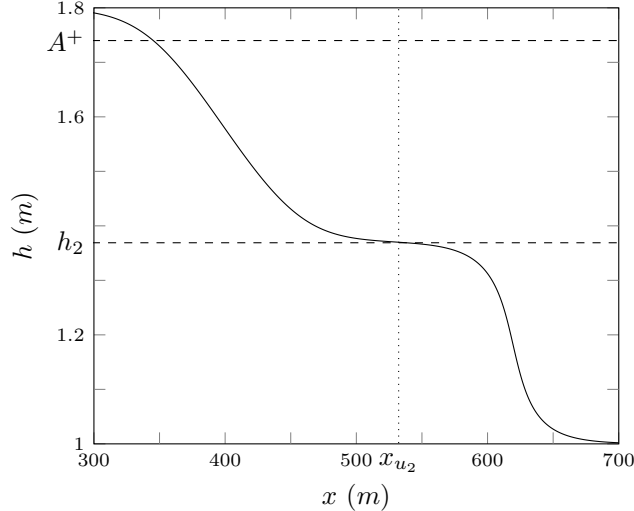


Figure 5: Numerical results of  $\mathcal{V}_3$  at  $t = 30s$  for the smooth dam-break problem with  $\alpha = 40m$  for  $\Delta x = 10/2^4 m$  (—).

solutions for higher  $\Delta x$  are visually identical. There is also good agreement between the peak amplitude in region IV ( $A$ ) and  $A^+$  as well as  $h(x_{u_2})$  and  $h_2$ . Although as  $\Delta x$  is decreased in the simulations we observe  $h(x_{u_2}) > h_2$ . These solutions replicate the structure of the numerical solutions of Mitsotakis et al. [4] who use the same  $\alpha$  but different  $h_0$  and  $h_1$ .

Table 1 demonstrates good conservation of the conserved quantities for our numerical solution with  $\Delta x = 10/2^{10} m$ , although only the errors in conservation of  $h$  are at the size of round-off errors. The  $L_1$  measures demonstrate that the numerical solutions in Figure 6 are very close to the numerical solution with  $\Delta x = 10/2^{11} m$ .

#### 270 5.1.3. Node Structure

271 The third structure will be referred to as the node structure and it was observed by  
 272 [1]. The node structures main feature is that the oscillations in region III and IV decay  
 273 and appear to meet at  $x_{u_2}$  as can be seen in Figure 7 when  $\alpha = 0.4m$ . Unfortunately  
 274 these numerical solutions are not visually identical for the higher resolutions as they  
 275 were in the flat structure example. However, the numerical solutions are getting closer  
 276 to one another and convergence is expected for the smaller  $\Delta x$  because the problem is  
 277 still smooth. In these results  $A^+$  is a good estimator for  $A$  and the oscillations in regions  
 278 III and IV appear to be around  $h_2$ . This structure was observed by [1] for  $\mathcal{E}$  and indeed  
 279 we have replicated it.

280 This structure was not observed in  $\mathcal{V}_1$ 's solutions up to  $\Delta x = 10/2^{10} m$  with  $\alpha =$   
 281  $0.001m$  as  $\mathcal{V}_1$  introduces numerical diffusion that severely dampen oscillations. This  
 282 explains why the numerical solutions of Le Métayer et al. [2] using  $\mathcal{V}_1$  have a different  
 283 structure to those of El et al. [1]. It was found that an  $\alpha$  of at least  $0.4m$  is required  
 284 to recover the node structure which explains why Mitsotakis et al. [3] and Mitsotakis  
 285 et al. [4] using  $\alpha$ 's of  $2m$  and  $1m$  respectively could not reproduce the structure of the

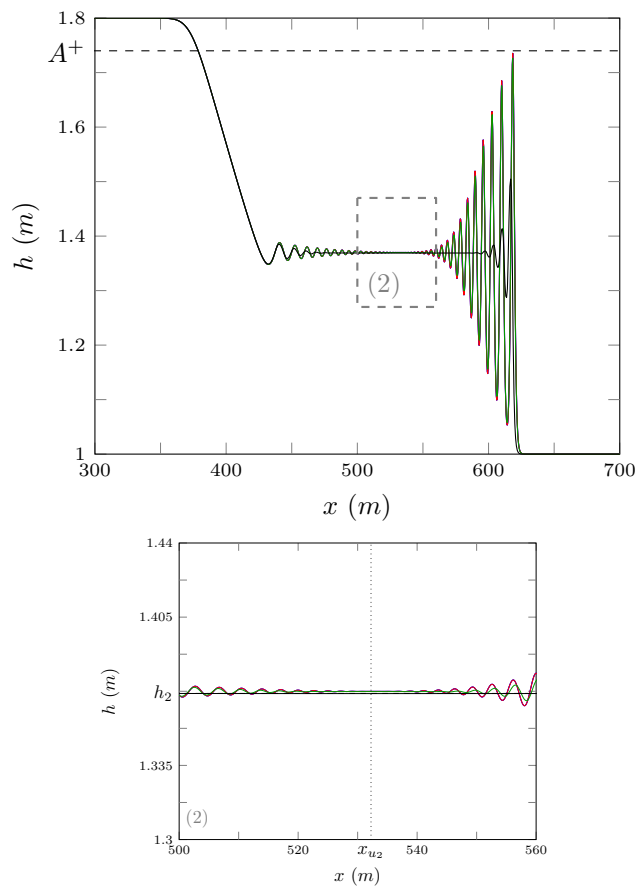


Figure 6: Numerical results of  $\mathcal{V}_3$  at  $t = 30s$  for the smooth dam-break problem with  $\alpha = 2m$  for  $\Delta x = 10/2^{10}m$  (—),  $10/2^8m$  (—),  $10/2^6m$  (—) and  $10/2^4m$  (—).

286 numerical solutions of El et al. [1].

287 Figure 7 demonstrates that our numerical solutions have not converged, however  
288 this is only in the area around  $x_{u_2}$ . This indicates that our solutions away from  $x_{u_2}$  are  
289 consistent, in particular our results for  $A$ . The larger distance between numerical solu-  
290 tions means we cannot get a meaningful measure of  $L_1$  for the whole domain. However,  
291 by omitting an interval around  $x_{u_2}$  such as  $[520m, 540m]$  a meaningful measure of  $L_1$   
292 can be calculated, this modified  $L_1$  is presented in Table 1. These modified  $L_1$ 's demon-  
293 strate that our solutions are close to one another and have converged away from  $x_{u_2}$ , so  
294 that increasing the grid resolution further would only cause a significant change in the  
295 numerical solutions around  $x_{u_2}$ . Table 1 shows that for  $\Delta x = 10/2^{10}m$  our conserved  
296 quantities are very well conserved by our numerical solution.

297 These results suggest that although we have not yet fully converged these numerical  
298 solutions are close to reasonable solutions of the Serre equations for the smoothed dam-  
299 break problem for an appropriate  $\alpha$  value supporting the structure of the numerical  
300 solutions presented by El et al. [1].

#### 301 5.1.4. Growth Structure

302 The fourth structure will be referred to as the growth structure due to the oscillations  
303 in regions III and IV growing around  $x_{u_2}$  as can be seen in Figure 8 for  $\alpha = 0.1m$ . This  
304 structure could not be replicated for  $\mathcal{V}_1$  and has hitherto not been published.

305 Figure 8 shows that the disagreement in the numerical results is concentrated around  
306  $x_{u_2}$ .  $A$  is again predicted by  $A^+$  well and the oscillations in regions III and IV are around  
307  $h_2$ . The different resolution numerical results are getting closer to one another, but the  
308 sudden change in structure around  $x_{u_2}$  makes it difficult to assert that large growths  
309 in amplitude are not possible around  $x_{u_2}$  as we take  $\Delta x$  smaller. However, for nu-  
310 mercial solutions with  $\alpha = 0.001m$  and  $\Delta x = 10/2^{11}m$  these oscillations around  $x_{u_2}$   
311 stayed within the interval  $[1.3m, 1.455m]$ . The number of oscillations is the same for  
312  $\Delta x = 10/2^{10}m$  in Figures 7 and 8 with different  $\alpha$  values so that the change in structure  
313 is a result of the difference in amplitudes of the oscillations and not an increase in their  
314 number.

315 The interval  $[520m, 540m]$  has been omitted from  $L_1$  in Table 1 due to the lack of  
316 convergence in this region. The  $L_1$  measures for the numerical solution with  $\alpha = 0.1m$   
317 and  $\Delta x = 10/2^{10}m$  are very close but slightly larger than those for the node structure,  
318 confirming that our numerical solutions are correctly capturing the behaviour of the  
319 Serre equations for this problem away from  $x_{u_2}$ . The errors in conservation are small,  
320 and in particular our conservation of  $h$  is as good as those in node and flat structures.  
321 The errors in conservation of  $uh$  and  $\mathcal{H}$  however are larger than the previous structures  
322 examples by a factor of 10.

323 Since this structure in numerical solutions cannot be found in the literature and the  
324 numerical solutions exemplifying that structure have poorer convergence and conser-  
325 vation than any other examples we resort to using many different methods to support  
326 the numerical solutions of  $\mathcal{V}_3$ . To remove the possibility that some effect from the re-  
327 formulation of the Serre equations or the elliptic solver of the  $\mathcal{V}_i$  methods are the cause  
328 we use make use of  $\mathcal{G}$  and  $\mathcal{E}$ .  $\mathcal{G}$ ,  $\mathcal{E}$ ,  $\mathcal{V}_1$  and  $\mathcal{V}_3$  are applied to the same initial conditions  
329 with the same grid resolutions as above and the results were plotted in Figure 9.  $\mathcal{V}_2$   
330 has been omitted from this figure for clarity because its solution is very close to  $\mathcal{V}_3$ .

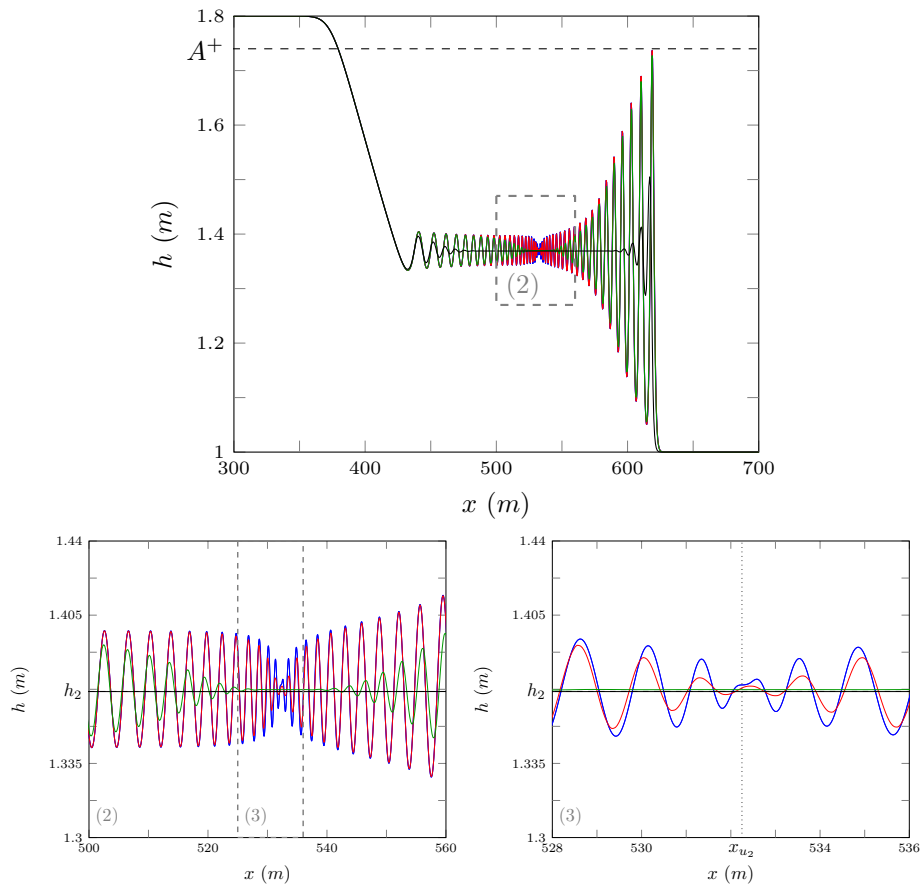


Figure 7: Numerical results of  $\mathcal{V}_3$  at  $t = 30s$  for the smooth dam-break problem with  $\alpha = 0.4m$  for  $\Delta x = 10/2^{10}m$  (—),  $10/2^8m$  (—),  $10/2^6m$  (—) and  $10/2^4m$  (—).

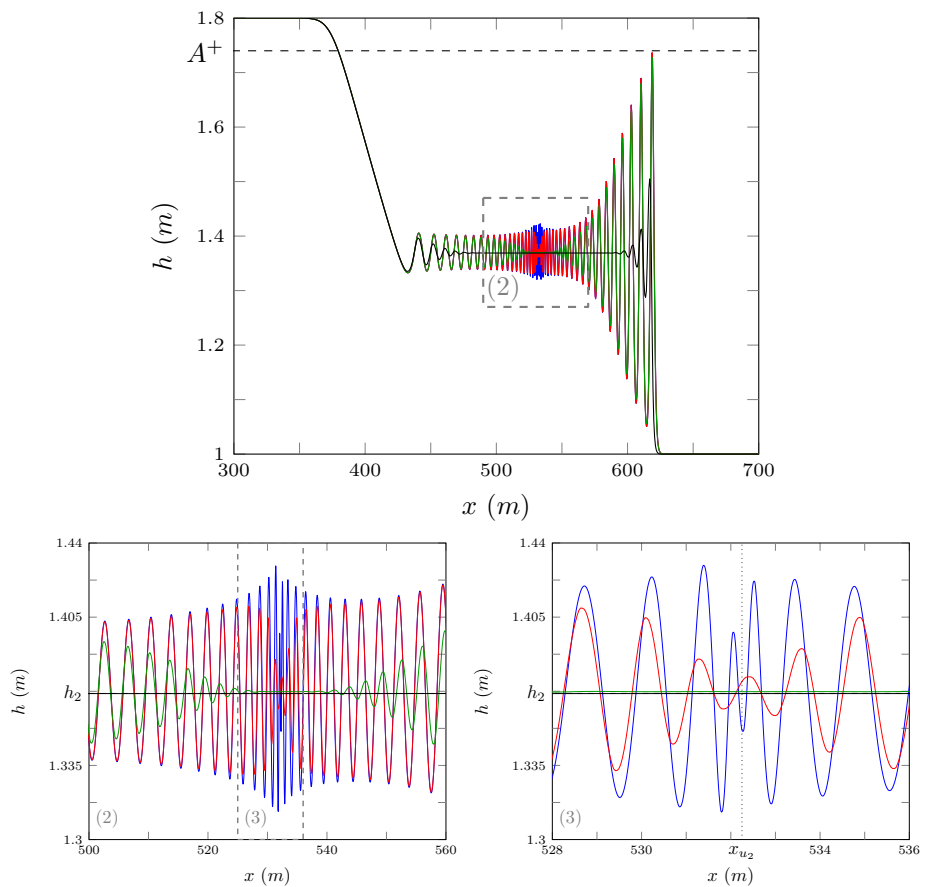


Figure 8: Numerical results of  $\mathcal{V}_3$  at  $t = 30s$  for the smooth dam-break problem with  $\alpha = 0.1m$  for  $\Delta x = 10/2^{10}m$  (—),  $10/2^8m$  (—),  $10/2^6m$  (—) and  $10/2^4m$  (—).

331     The first observation is that  $\mathcal{V}_1$  has not recovered a growth structure. This is be-  
332     cause  $\mathcal{V}_1$  is very diffusive [5], dampening these oscillations. To resolve this structure  
333     for  $\mathcal{V}_1$  would require restrictively small  $\Delta x$  and as such this has not been observed in  
334     the simulations. Secondly, all high-order methods recover this growth structure and  
335     disagree only in the region around  $x_{u_2}$ . The absence of the growth structure in the  
336     findings of El et al. [1] is the result of smoothing of the initial conditions [13].

337     Generally dispersive methods overestimate the size and number of oscillations of  
338     the true solution while diffusive methods underestimate the size and number of oscil-  
339     lations in the true solution. Since  $\mathcal{V}_3$  is diffusive as can be seen in Figure 8 and  $\mathcal{G}$   
340     is dispersive the true analytic solution should exist between  $\mathcal{V}_3$  and  $\mathcal{G}$ . As  $\mathcal{G}$  and  $\mathcal{V}_3$   
341     have the same number of oscillations we expect that the true solution will have the  
342     same number of oscillations with different amplitudes.

343     These results demonstrate that while our numerical results have not converged as  
344      $\Delta x \rightarrow 0$  the agreement of all the discussed methods of sufficiently high order indicates  
345     that these results are representative of actual solutions of the smoothed dam-break prob-  
346     lem with low  $\alpha$  for the Serre equations. This is the same structure that we observe for  
347      $\mathcal{V}_2$  and  $\mathcal{V}_3$  with the same  $\Delta x$  and  $\Delta t$  for the dam-break.

#### 348     5.1.5. Long Time

349     To assess long term behaviour of the numerical solutions a smoothed dam-break  
350     was solved by  $\mathcal{V}_3$  with the same parameters on a larger domain  $x \in [-900m, 1800m]$   
351     for a longer time  $t \in [0, 300s]$ . The results of  $\mathcal{V}_3$  with  $\alpha = 0.1m$  and  $\Delta x = 10/2^9 m$  and  
352      $10/2^8 m$  at  $t = 300s$  are presented in Figure 10. For this problem these parameters result  
353     in the growth structure at  $t = 30s$ , however after sufficient time this growth structure  
354     has decayed into a flat structure although there are still small oscillations present in the  
355     middle region.

356     To track the decaying of the oscillations for  $\mathcal{V}_3$ 's solution around  $x_{u_2}$  a snapshot  
357     of the area around  $x_{u_2}$  has been plotted for different times in Figure 11. It can be seen  
358     that at  $t = 30s$  the solution exhibits the growth structure but as time progresses the  
359     region around  $x_{u_2}$  has decayed into the node structure by  $t = 100s$  and then into the flat  
360     structure observed at  $t = 200s$  and  $t = 300s$ .

361     By considering the Fourier series of the smoothed dam-break the underlying pro-  
362     cess at work in the numerical solutions of the smoothed approximation of the dam-  
363     break Serre equations can be understood. At  $t = 0$  the contact discontinuity is at  $x_0$   
364     as time progresses and the fluid on the left side rushes to fill the right side the Fourier  
365     components with lowest  $k$  propagate away from the contact discontinuity due to the  
366     different phase velocities. The Fourier components corresponding to larger and larger  
367      $k$  continue to propagate away from the contact discontinuity but travel slower than the  
368     oscillations corresponding to lower  $k$  as the phase velocity is closer to the mean bore  
369     speed. Because the initial conditions are smooth and a numerical method is used are a  
370     bounded number of Fourier components in the Fourier series that will be produced by  
371     our numerical solutions resulting in a constant state around the contact discontinuity.  
372     Thus for our numerical solutions the growth structure will decay into the node structure  
373     which will decay into the flat structure over sufficient time.

374     However, we have not seen all the oscillations present in  $\alpha = 0.1m$  at  $t = 300s$  as  
375     Figure 10 demonstrates that over this time span we are not close to convergence of the

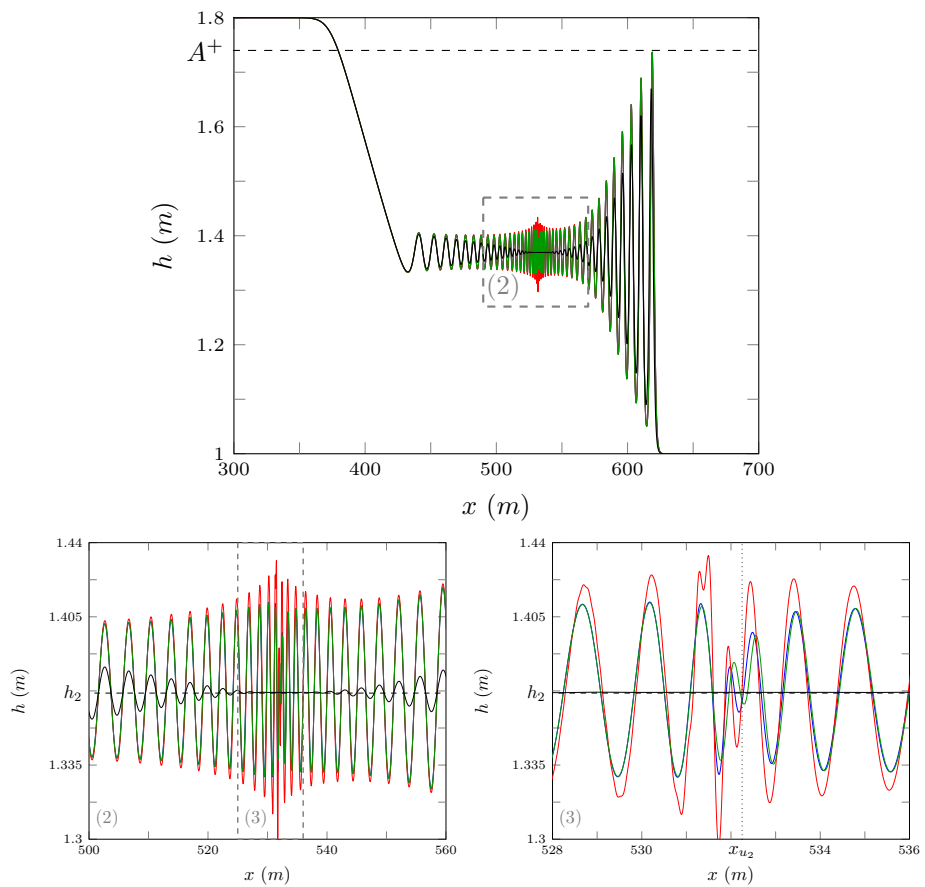


Figure 9: Numerical results for the smooth dam-break problem with  $\alpha = 0.1m$  and  $\Delta x = 10/2^{10}m$  for  $\mathcal{G}$  (—),  $\mathcal{E}$  (—),  $\mathcal{V}_3$  (—) and  $\mathcal{V}_1$  (—).

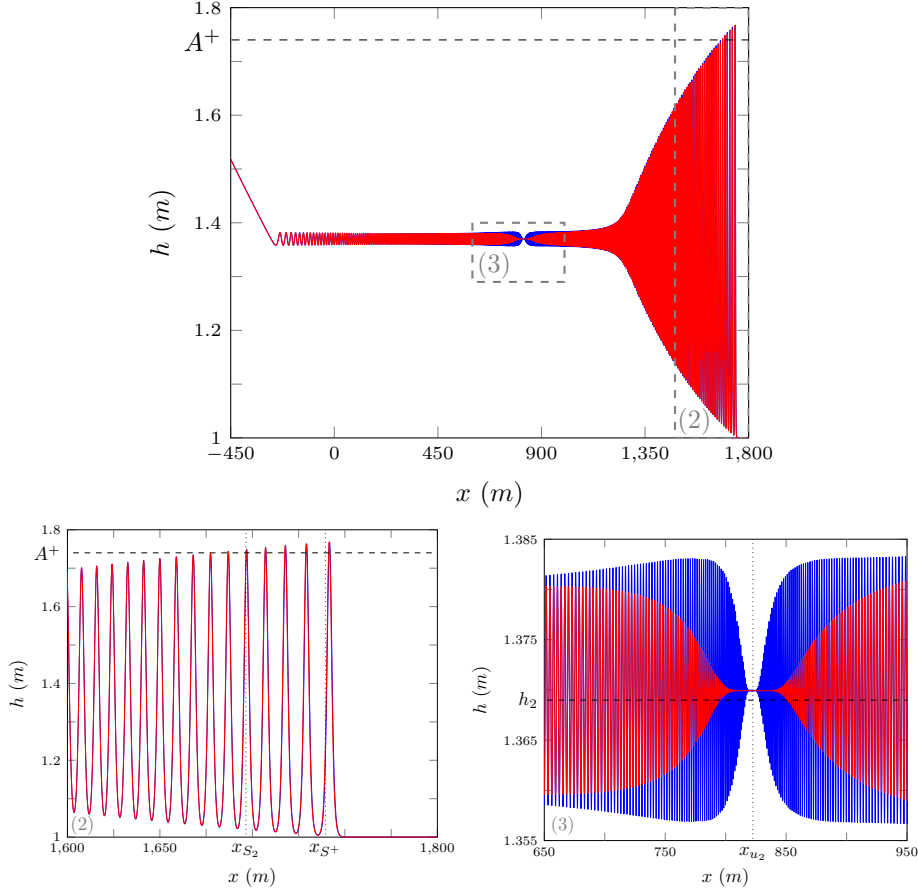


Figure 10: Numerical solution of smooth dam-break problem at  $t = 300s$  by  $\mathcal{V}_3$  with  $\alpha = 0.1m$  for  $\Delta x = 10/2^9 m$  (blue) and  $10/2^8 m$  (red).

376 numerical results.

377 *5.2. Shallow water wave equation comparison*

378 The analytic solutions of shallow water wave equations have been used as a guide  
 379 for the mean behaviour of the solution of the Serre equations for the dam-break problem  
 380 in the literature [2, 3]. Since it has been demonstrated that the contact discontinuity  
 381 travels at the mean velocity inside the bore we can assess how well  $u_2$  approximates  
 382 the mean velocity inside the bore by measuring the speed of the contact discontinuity  
 383 and comparing it to  $u_2$ . This was done for a range of different bore speeds by changing  
 384 the aspect ratio of the smoothed dam-break problem by fixing  $h_0 = 1m$  and varying  $h_1$   
 385 to allow for different mean velocities inside the bore. The results of this process are  
 386 plotted in Figure 12 which confirms that the contact discontinuity travels at speed  $u_2$   
 387 for a range of aspect ratios.

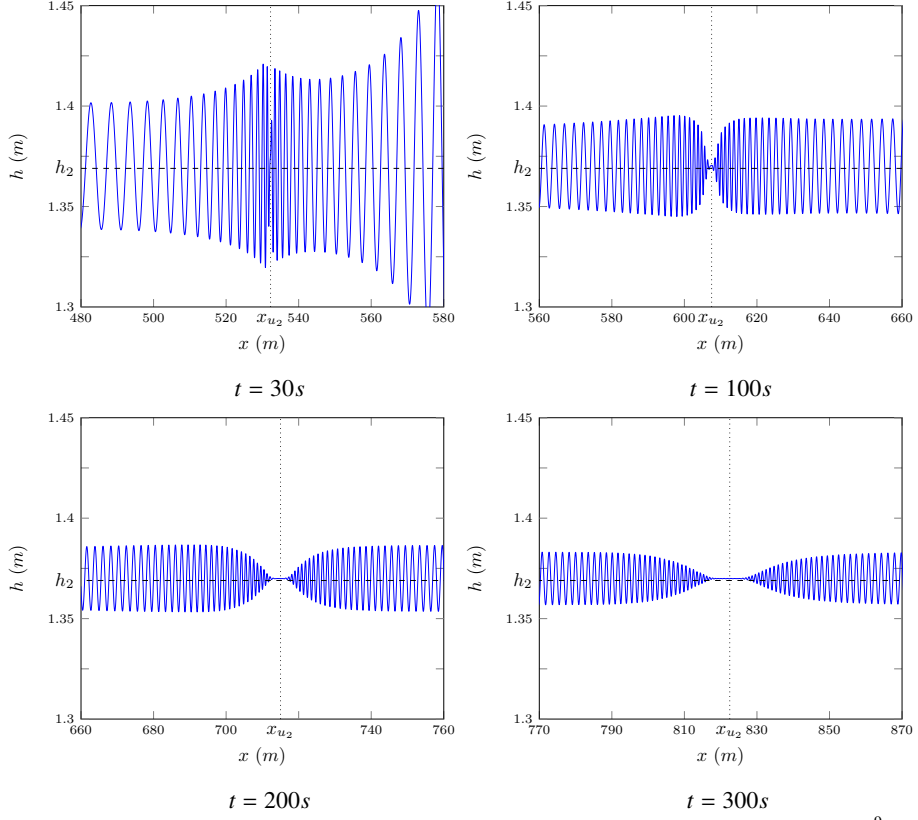


Figure 11: Numerical solution of the smooth dam-break problem by  $\mathcal{V}_3$  with  $\alpha = 0.1\text{m}$  and  $\Delta x = 10/2^9\text{m}$  at various times.

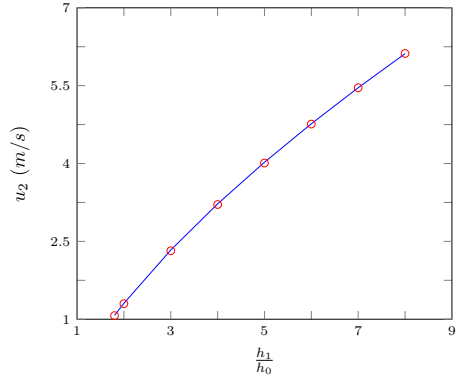


Figure 12:  $u_2$  (—) and speed of the contact discontinuity (○) for numerical solutions of smoothed dam-break problems with different aspect ratios ( $h_1/h_0$ ) by  $\mathcal{V}_3$  where  $\alpha = 0.1\text{m}$  and  $\Delta x = 10/2^9\text{m}$  at  $t = 100\text{s}$ .

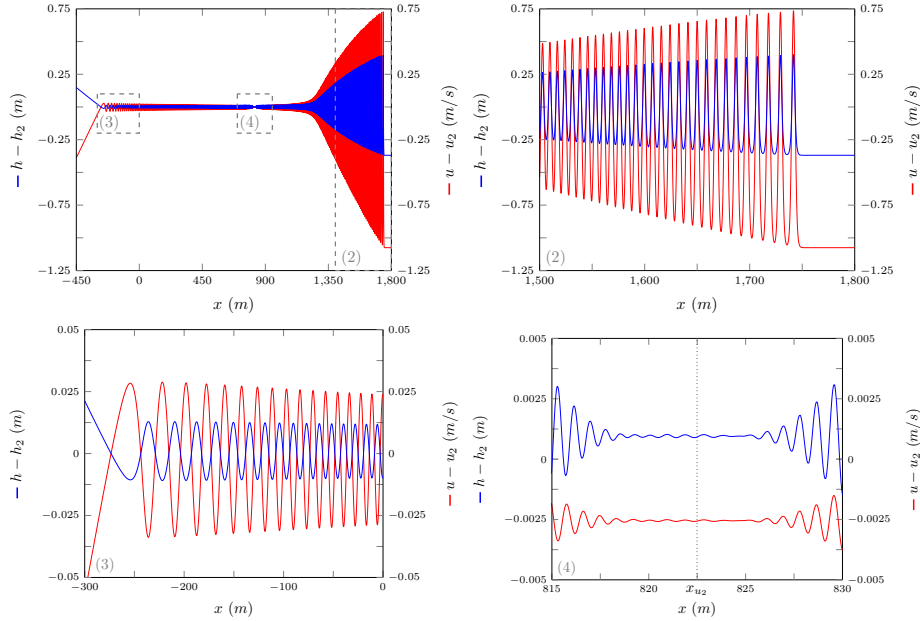


Figure 13:  $h - h_2$  (blue) and  $u - u_2$  (red) for numerical solution of the smooth dam-break by  $\mathcal{V}_3$  with  $\alpha = 0.1m$  and  $\Delta x = 10/2^9 m$  at  $t = 300s$  as in Figure 10.

The applicability of the analytic solutions can also be assessed by plotting  $h - h_2$  and  $u - u_2$  which has been performed for the smoothed dam-break problem with  $\alpha = 0.1m$  and  $\Delta x = 10/2^9 m$  in Figure 13 for  $t = 300s$ . From this figure it can be seen that the mean velocity and height of the bore are slightly different from the shallow water wave equation values  $h_2$  and  $u_2$ . With  $h_2$  being an underestimate and  $u_2$  being an overestimate. We can also see that  $u_2$  is an overestimate for the speed of the contact discontinuity as  $h - h_2$  and  $u - u_2$  are in-phase at  $x_{u_2}$  thus  $x_{u_2}$  is to the right of the contact discontinuity. Figure 10 demonstrates that  $S_2$  is a poor approximation to the speed of the bore.

### 5.3. Whitham modulation comparison

The expressions for the leading wave amplitude  $A^+$  and speed  $S^+$  obtained by [1] are asymptotic results and so we are interested in how our numerical results behave over time. Thus for the dam-break problem in Figure 10 the peak amplitude in region IV (A) was plotted over time in Figure 14. It can be seen that  $A$  approaches a value larger than  $A^+$  over time. We find that as  $\alpha \rightarrow 0$  and  $\Delta x \rightarrow 0$   $A$  converges away from  $A^+$  in this time scale for this aspect ratio. Thus it appears that the true solution of the dam-break for the Serre equations has an amplitude in region IV slightly above  $A^+$ . This is not inconsistent with the results of [1] as their scale comparing  $A^+$  to  $A$  is too large to see such a small difference. From Figure 10 it can be seen that while  $S^+$  does not precisely predict the bore speed it is a better prediction than  $S_2$ .

These results together with those of El et al. [1] demonstrate that  $A$  and  $A^+$  are highly correlated across a range of different smoothed dam-break problems, but for a

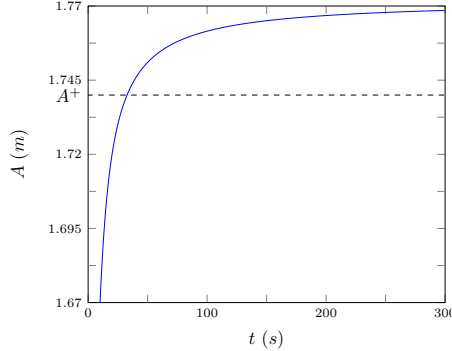


Figure 14: Leading wave height plotted over time for the numerical solution of the smooth dam-break problem by  $\mathcal{V}_3$  with  $\alpha = 0.1m$  for  $\Delta x = 10/2^9 m$  (—) as in Figure 10.

410 given problem these two are not precisely equal for our numerical results.

411 **6. Conclusions**

412 Utilising two finite difference methods of second-order and three finite difference-  
 413 volume hybrid methods of various orders an investigation into the smoothed dam-break  
 414 problem with varying steepness was performed. Four different structures of the numer-  
 415 ical solutions were uncovered with the general trend being that an increase in steepness  
 416 increases the size and number of oscillations in the solution. This study explains the  
 417 different numerical results in literature involving the solution of the Serre equations  
 418 applied to the smoothed dam-break problem and also uncovers a new result. We find  
 419 that while the analytic solution of the shallow water wave equations for the dam-break  
 420 problem is a good guide to the mean behaviour of the Serre equations the speed and  
 421 height of the bores do not match up precisely. While the Whitham modulation results  
 422 for the Serre equations give better predictions than the shallow water wave equations  
 423 analytic solution it was found that they also do not line up with our numerical results  
 424 precisely. Lastly, it was demonstrated that the contact discontinuity corresponds to high  
 425 wave numbers and thus travels at the mean velocity inside the bore.

- 426 [1] G. El, R. H. J. Grimshaw, N. F. Smyth, Unsteady undular bores in fully nonlinear  
 427 shallow-water theory, *Physics of Fluids* 18 (027104).
- 428 [2] O. Le Métayer, S. Gavrilyuk, S. Hank, A numerical scheme for the GreenNaghdi  
 429 model, *Journal of Computational Physics* 229 (6) (2010) 2034–2045.
- 430 [3] D. Mitsotakis, B. Ilan, D. Dutykh, On the Galerkin/Finite-Element Method for  
 431 the Serre Equations, *Journal of Scientific Computing* 61 (1) (2014) 166–195.
- 432 [4] D. Mitsotakis, D. Dutykh, J. Carter, On the nonlinear dynamics of the traveling-  
 433 wave solutions of the Serre system, *Wave Motion* 70 (1) (2017) 166–182.
- 434 [5] C. Zoppou, J. Pitt, S. Roberts, Numerical Solution of the Fully Non-linear Weakly  
 435 Dispersive Serre Equations for Steep Gradient Flows, *Applied Mathematical  
 436 Modelling* 00 (00) (2017) 00–00.

- 437 [6] C. H. Su, C. S. Gardner, Korteweg-de Vries equation and generalisations. III.  
 438 Derivation of the Korteweg-de Vries equation and Burgers equation, Journal of  
 439 Mathematical Physics 10 (3) (1969) 536–539.
- 440 [7] D. Lannes, P. Bonneton, Derivation of asymptotic two-dimensional time-  
 441 dependent equations for surface water wave propagation, Physics of Fluids 21 (1)  
 442 (2009) 16601–16610.
- 443 [8] M. Li, P. Guyenne, F. Li, L. Xu, High order well-balanced CDG-FE methods  
 444 for shallow water waves by a Green-Naghdi model, Journal of Computational  
 445 Physics 257 (2014) 169–192.
- 446 [9] Y. A. Li, Hamiltonian Structure and Linear Stability of Solitary Waves of the  
 447 Green-Naghdi Equations, Journal of Nonlinear Mathematical Physics 9 (2002)  
 448 99–105.
- 449 [10] A. E. Green, P. M. Naghdi, A derivation of equations for wave propagation in  
 450 water of variable depth, Journal of Fluid Mechanics 78 (2) (1976) 237–246.
- 451 [11] A. A. Harten, High resolution schemes for hyperbolic conservation laws, Journal  
 452 of Computational Physics 49 (3) (1983) 357–393.
- 453 [12] C. Wu, G. Huang, Y. Zheng, Theoretical solution of dam-break shock wave, Jour-  
 454 nal of Hydraulic Engineering 125 (11) (1999) 1210–1215.
- 455 [13] G. El, M. Hoefer, Dispersive shock waves and modulation theory, Physica D:  
 456 Nonlinear Phenomena 333 (2016) 11–65.

457 **Appendix A.**

458  $\mathcal{E}$  and  $\mathcal{G}$  use the centred second-order finite difference approximation to the con-  
 459 servation of momentum equation (1b) denoted as  $\mathcal{G}_u$ . For the conservation of mass  
 460 equation (1a)  $\mathcal{E}$  uses the two step Lax-Wendroff method denoted as  $\mathcal{E}_h$  while  $\mathcal{G}$  uses a  
 461 centred second-order finite difference approximation denoted as  $\mathcal{G}_h$ .

462 *Appendix A.1.  $\mathcal{G}_u$  for Conservation of Momentum Equation*

463 The finite difference approximation to (1b) on our grid is

$$464 \quad h_i^n u_i^{n+1} - (h_i^n)^2 \left( \frac{u_{i+1}^{n+1} - u_{i-1}^{n+1}}{2\Delta x} \right) - \frac{(h_i^n)^3}{3} \left( \frac{u_{i+1}^{n+1} - 2u_i^{n+1} + u_{i-1}^{n+1}}{\Delta x^2} \right) = -Y_i^n \quad (\text{A.1})$$

466 and

$$467 \quad Y_i^n = 2\Delta t X_i^n - h_i^n u_i^{n-1} + (h_i^n)^2 \left( \frac{u_{i+1}^{n-1} - u_{i-1}^{n-1}}{2\Delta x} \right) + \frac{(h_i^n)^3}{3} \left( \frac{u_{i+1}^{n-1} - 2u_i^{n-1} + u_{i-1}^{n-1}}{\Delta x^2} \right).$$

469 Equation (A.1) can be rearranged into an explicit update scheme  $\mathcal{G}_u$  for  $u$  given its  
 470 current and previous values, so that

$$471 \quad \begin{bmatrix} u_0^{n+1} \\ \vdots \\ u_m^{n+1} \end{bmatrix} = A^{-1} \begin{bmatrix} -Y_0^n \\ \vdots \\ -Y_m^n \end{bmatrix} =: \mathcal{G}_u(\mathbf{u}^n, \mathbf{h}^n, \mathbf{u}^{n-1}, \Delta x, \Delta t) \quad (A.2)$$

472

473 where  $A$  is a tri-diagonal matrix.

474 *Appendix A.2. Numerical Methods for Conservation of Mass Equation*

475 *Appendix A.2.1.  $\mathcal{E}_h$*

476 The two step Lax-Wendroff update  $\mathcal{E}_h$  for  $h$  is

$$477 \quad h_{i+1/2}^{n+1/2} = \frac{1}{2} (h_{i+1}^n + h_i^n) - \frac{\Delta t}{2\Delta x} (u_{i+1}^n h_{i+1}^n - h_i^n u_i^n),$$

478

$$480 \quad h_{i-1/2}^{n+1/2} = \frac{1}{2} (h_i^n + h_{i-1}^n) - \frac{\Delta t}{2\Delta x} (u_i^n h_i^n - h_{i-1}^n u_{i-1}^n)$$

481

482 and

$$483 \quad h_i^{n+1} = h_i^n - \frac{\Delta t}{\Delta x} (u_{i+1/2}^{n+1/2} h_{i+1/2}^{n+1/2} - u_{i-1/2}^{n+1/2} h_{i-1/2}^{n+1/2}).$$

484

485 The quantities  $u_{i\pm 1/2}^{n+1/2}$  are calculated using  $u^{n+1}$  obtained by applying  $\mathcal{G}_u$  (A.2) to  $u^n$  then  
 486 linearly interpolating in space and time to give

$$487 \quad u_{i+1/2}^{n+1/2} = \frac{u_{i+1}^{n+1} + u_{i+1}^n + u_i^{n+1} + u_i^n}{4}$$

488

489 and

$$490 \quad u_{i-1/2}^{n+1/2} = \frac{u_i^{n+1} + u_i^n + u_{i-1}^{n+1} + u_{i-1}^n}{4}.$$

491

492 Thus we have the following update scheme  $\mathcal{E}_h$  for (1a)

$$493 \quad \mathbf{h}^{n+1} = \mathcal{E}_h(\mathbf{u}^n, \mathbf{h}^n, \mathbf{u}^{n+1}, \Delta x, \Delta t). \quad (A.3)$$

494

495 *Appendix A.2.2.  $\mathcal{G}_h$*

496 The second order centered finite difference approximation to the conservation of  
 497 mass equation (1a) is

$$498 \quad h_i^{n+1} = h_i^{n-1} - \Delta t \left( u_i^n \frac{h_{i+1}^n - h_{i-1}^n}{\Delta x} + h_i^n \frac{u_{i+1}^n - u_{i-1}^n}{\Delta x} \right).$$

499

500 Thus we have an update scheme  $\mathcal{G}_h$  for all  $i$

$$501 \quad \mathbf{h}^{n+1} = \mathcal{G}_h(\mathbf{u}^n, \mathbf{h}^n, \mathbf{h}^{n-1}, \Delta x, \Delta t). \quad (A.4)$$

502

503    *Appendix A.3.  $\mathcal{E}$*

504     $\mathcal{E}$  is the combination of (A.3) for (1a) and (A.2) for (1b) in the following way

$$505 \quad \begin{aligned} \mathbf{u}^{n+1} &= \mathcal{G}_u(\mathbf{u}^n, \mathbf{h}^n, \mathbf{u}^{n-1}, \Delta x, \Delta t) \\ \mathbf{h}^{n+1} &= \mathcal{E}_h(\mathbf{u}^n, \mathbf{h}^n, \mathbf{u}^{n+1}, \Delta x, \Delta t) \end{aligned} \quad \left. \right\} \mathcal{E}(\mathbf{u}^n, \mathbf{h}^n, \mathbf{u}^{n-1}, \mathbf{h}^{n-1}, \Delta x, \Delta t). \quad (\text{A.5})$$

506

507    *Appendix A.4.  $\mathcal{G}$*

508     $\mathcal{G}$  is the combination of (A.4) for (1a) and (A.2) for (1b) in the following way

$$509 \quad \begin{aligned} \mathbf{h}^{n+1} &= \mathcal{G}_h(\mathbf{u}^n, \mathbf{h}^n, \mathbf{h}^{n-1}, \Delta x, \Delta t) \\ \mathbf{u}^{n+1} &= \mathcal{G}_u(\mathbf{u}^n, \mathbf{h}^n, \mathbf{u}^{n-1}, \Delta x, \Delta t) \end{aligned} \quad \left. \right\} \mathcal{G}(\mathbf{u}^n, \mathbf{h}^n, \mathbf{u}^{n-1}, \mathbf{h}^{n-1}, \Delta x, \Delta t). \quad (\text{A.6})$$

510